Preparation and Mechanisms of Core-Shell Hierarchical Porous Composites for Targeted Enrichment and Protection of AnAOB

Jiaqi Yan [a], Yongrong Jiang [a], Yongli Qin [a, *], Ruihong Chen [a], Mingming Li [a], Minglin Wu [a], You Wu [a]

[a] *School of Life and Environmental Sciences, Guilin University of Electronic Technology, Guilin, 541004, China*

[*] Corresponding author.

E-mail addresses: qinyongli0318@sina.com (Y. Qin).

S1 Experiment

S1.1 Materials

Biochar (BC), made by pyrolysis of corn stalks at 600°C, Green Plains Activated Carbon Co., Ltd; NaY-type molecular sieve (MS), pore size: 0.74 nm, average particle size: 1~3 μm, Chemical Operation Department; Ferric chloride, analytically pure, Xilong Chemical Reagent Co., Ltd.

S1.2 Screening of BFMS-*x* composite

To identify the optimal molecular sieve loading ratio, BFMS-*x* composites with different shell loadings (*x* = 0%, 30%, 60%, and 100%) were evaluated through AnAOB enrichment tests and resistance assays under Cu (II) and TCE stress.

All batch experiments were conducted in 200 mL serum bottles under identical operating conditions. The initial concentrations of substrates were 100 $mg \cdot L^{-1}$ NH_4^+-N and 132 $mg \cdot L^{-1}$ NO_2^--N, with an initial pH of 7.03 and an incubation temperature of 35 °C. Dissolved oxygen was removed by purging the solution with N_2 for 10 min prior to incubation. Dissolved oxygen was reduced by purging the solution with N_2 for 10 min, 35℃. BFMS-*x* composites with different molecular sieve loading ratios were sampled at 2 mL each and mixed with equal volumes (10 mL) of Anammox sludge with identical activity (VSS = 1860 $mg \cdot L^{-1}$), while a no-material group served as the control. After the enrichment stage, each serum bottle was successively spiked with 5 $mg \cdot L^{-1}$ Cu (II) and 1 $mg \cdot L^{-1}$ TCE to simulate combined heavy-metal and antibiotic stress.

During the reaction, liquid samples were collected hourly, and the temporal variations in NH_4^+-N, NO_2^--N, and NO_3^--N concentrations were continuously monitored. Based on the comparative results for growth promotion and resistance under inhibitory stress, the optimal BFMS was identified. All experiments were conducted in triplicate.

S1.3 Mechanism-verification experiments

To investigate the enrichment-promoting and protective mechanisms of BFMS toward AnAOB, a total of 14 interaction systems were constructed using different carrier materials (BK, MS, BF, and BFMS) in combination with AnAOB (Table 1). In all systems, the initial substrate concentrations were set at NH_4^+-N 100 $mg \cdot L^{-1}$ and NO_2^--N 132 $mg \cdot L^{-1}$.

Systems I-VIII were operated without Cu(II) and TCE to evaluate the effects of different carriers on AnAOB enrichment and substrate conversion. Systems IX-XIV

were operated under combined Cu(II)-TCE stress to assess the protective effects of different carriers against inhibitory compounds. In the stress-response systems, the initial concentrations of Cu(II) and TCE were set at 5 $mg \cdot L^{-1}$ and 1 $mg \cdot L^{-1}$, respectively.

To examine whether soluble Fe released from carrier materials could influence AnAOB activity, a blank control and a BFMS-only group were further established under identical water-composition conditions to determine Fe leaching concentrations. These control experiments were used to distinguish the possible contribution of dissolved Fe from the structural protection effect of BFMS.

In addition, TCE concentrations were determined using high-performance liquid chromatography (HPLC, LC-2030C 3D Plus, Shimadzu, Japan). The concentration of Cu ions was measured by flame atomic absorption spectrometry (FAAS, PinAAcle 900T, PerkinElmer, USA).

S1.4 DFT analysis

Structural optimization and electronic structure calculations were performed within the framework of density functional theory (DFT) using the Vienna ab initio Simulation Package (VASP). The projector augmented-wave (PAW) method was employed to describe the electron-ion interactions, together with the Perdew-Burke-Ernzerhof (PBE) exchange-correlation functional within the generalized gradient approximation (GGA). For the biochar-Fe (BC-Fe) interfacial model, the Brillouin zone was sampled using a Γ-centered 2×2×1 *k*-point mesh. A plane-wave energy cutoff of 500 eV was applied. The electronic self-consistent calculations were converged to 10^{-5} eV per atom, and all lattice parameters and atomic positions were fully relaxed until the residual Hellmann-Feynman forces on each atom were below 0.03 $eV \cdot Å^{-1}$, ensuring a stable ground-state configuration.

Based on the optimized structures, projected density of states (PDOS) and charge-density difference analyses were carried out using the PBE functional. The choice of the PBE functional was motivated by its favorable balance between computational efficiency and accuracy, which is suitable for the extensive calculations required in this study. It is noted that PBE may systematically underestimate the intrinsic band gap of materials compared with experimental values or results obtained using hybrid functionals such as HSE06; however, this limitation does not affect the qualitative interpretation of interfacial electronic coupling and charge-transfer behavior discussed herein. Adsorption simulations were performed by placing Cu(II) ions and TCE

molecules approximately 3 Å above the BC-Fe surface, followed by analysis of adsorption energies and interfacial charge transfer.

In the simulation study of the TCE molecular system using the Gaussian16 and A03 software packages, the geometric optimization step employed the B3LYP functional with the def2-SVP basis set. This was combined with a polarizable continuous medium model to simulate the aqueous solvent environment, incorporating Grimme dispersion correction (GD3BJ). Subsequent single-point energy calculations employed the B3LYP functional with the def2-TZVP basis set, utilizing an electron-density-based solvent model to characterize water solvent effects, also incorporating Grimme dispersion correction. Calculations and analysis of frontier molecular orbitals (including the highest occupied molecular orbital, HOMO, and lowest unoccupied molecular orbital, LUMO), Fukui functions, and electrostatic potentials were performed using the Multiwfn program.

The Fukui function is a crucial concept in density functional theory for describing the local reactivity of a system. It is defined as the rate of change of the number of electrons with respect to the electronic density under constant external potential:

$$f(r)=\left[\frac{\partial_{\mu}}{\partial_{v}(r)}\right]_{N}=\left[\frac{\partial_{\rho}(r)}{\partial N}\right]_{v(r)} \quad \backslash* \text{ MERGEFORMAT (1.1)}$$

Here, N denotes the number of electrons in the system, ∂_{μ} represents the chemical potential of the system, $\partial_{v}(r)$ denotes the nuclear potential exerted on electrons, $\partial_{\rho}(r)$ represents the electron density, and ∂N denotes the number of electrons in the system. Depending on the reaction type, Fukui functions are typically defined in three forms:

Electrophilic attack (f^{-}): Describes the reactivity of a system when losing electrons, applicable for preicting sites of electrophilic reagent attack. The calculation formula is:

$$f^{-}(r)=\rho_{N}(r)-\rho_{N-1}(r)\approx\rho^{HOMO}(r) \quad \backslash* \text{ MERGEFORMAT (1.2)}$$

Nucleophilic Attack (f^{+}): Describes the reactivity of a system when acquiring electrons, applicable for predicting nucleophilic reagent attack sites. The calculation formula is:

$$f^{+}(r)=\rho_{N+1}(r)-\rho_{N}(r)\approx\rho^{LUMO}(r) \quad \backslash* \text{ MERGEFORMAT (1.3)}$$

Free radical attack (f^{0}): Describes the reactivity of a system in free radical

reactions, calculated as the arithmetic mean of the first two values:

$$f^0(r)=\frac{1}{2}\left[f^+(r)+f^-(r)\right]\approx\frac{1}{2}\left[\rho^{LUMO}+\rho^{HOMO}\right]\backslash*$$

MERGEFORMAT (1.4)

Among these, $\rho_N(r)$ $\rho_{N+1}(r)$ and $\rho_{N-1}(r)$ denote the electron density distributions of the system in neutral, anionic, and cationic states, respectively. Sites with higher Fukui function values are generally considered to possess greater local reactivity.

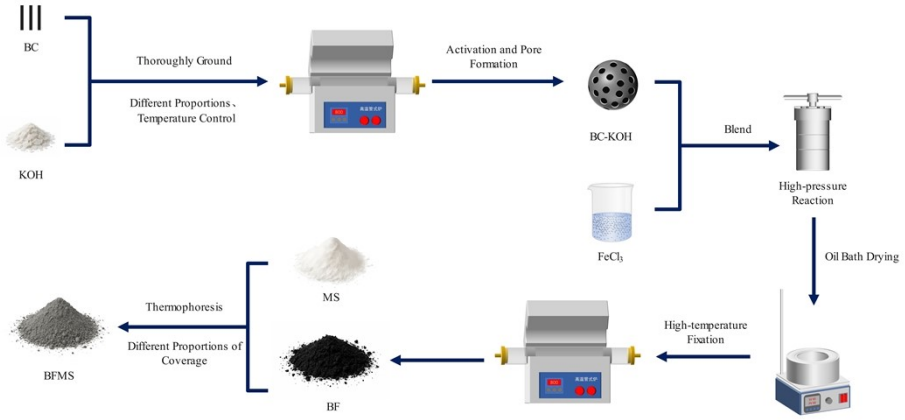

Figure S1. Preparation of BFMS

Table S1 Composition of BFMS-*x* composites and corresponding BF and MS volumes.

Composite	*x* (%)	BF (mL)	MS (mL)
BFMS-0%	0	5.0	0.0
BFMS-30%	30	5.0	1.5
BFMS-60%	60	5.0	3.0
BFMS-100%	100	5.0	5.0

S2 Results

S2.1 Nitrogen analysis and kinetic analysis

The concentrations of NO_2^--N, NO_3^--N, NH_4^+-N, MLSS, and MLVSS were measured using standard methods[1]. The temporal evolution of nitrogen concentrations was fitted with a first-order kinetic model[2], defined as:

$$C_t = C_0 \exp(-k \cdot t)$$

Where C_t is the nitrogen concentration ($mg \cdot L^{-1}$) at time t, C_0 is the initial concentration ($mg \cdot L^{-1}$), and k is the nitrogen removal rate constant (h^{-1}), which was used to evaluate the denitrification rate of the system.

S2.2 Determination of Fe(III) content and Haldane kinetic modeling

The Fe(III) content in lignocellulosic activated carbon was determined using standard analytical methods[3]. The Haldane model was applied to characterize substrate inhibition kinetics, and the inhibition effect of Fe(III) was modeled as follows[4]:

$$NRR = \frac{NRR_{max} \cdot S_{Fe}}{K_{Fe} + S_{Fe} + \frac{S_{Fe}^2}{K_I}}$$

Where NRR is the nitrogen removal rate ($kg \cdot (L \cdot d)^{-1}$), NRR_{max} is the maximum nitrogen removal rate ($kg \cdot (L \cdot d)^{-1}$), S_{Fe} is the influent Fe(III) concentration ($mg \cdot L^{-1}$), K_{Fe} is the half-saturation constant ($mg \cdot L^{-1}$), and K_I is the inhibition constant ($mg \cdot L^{-1}$).

S2.3 Calculation of exposure metrics

The trapezoidal rule was applied to numerically integrate the bulk-liquid concentration-time curves within a specified time window to obtain the cumulative exposure index (AUC). The concentration at C_{t1} was used as the baseline for normalization to calculate the residual fraction (R_{tn}) and the normalized cumulative exposure (AUC_{rel}), allowing comparison of inhibitor exposure among different interaction systems[5].

$$R_{t_n} = \frac{C_{t_n}}{C_{t_1}}$$

$$AUC_{t_1-t_n} \approx \sum_{i=1}^{n-1} \frac{C_i + C_{i+1}}{2} \left(t_{i+1} - t_i\right)$$

Normalisation:

$$AUC_{rel,t_1-t_n} \approx \sum_{i=1}^{n-1} \frac{\frac{C_i}{C_{t_1}} + \frac{C_{i+1}}{C_{t_1}}}{2} \left(t_{i+1} - t_i\right)$$

Where R_{tn} represents the ratio of the residual concentration at the endpoint relative to the baseline; $AUC_{t1\text{-}tn}$ represents the area under the concentration-time curve within the time window from t_1 to t_n (mg·L^{-1}·h); $AUC_{rel,t1\text{-}tn}$ denotes the relative cumulative exposure normalized by the concentration at time t_1 (h); C_t represents the concentration of the target component in the bulk liquid at time t (mg·L^{-1}); C_i and C_{i+1} represent the concentrations at times t_i and t_{i+1}, respectively (mg·L^{-1}); t, t_i, and t_{i+1} represent time points (h); t_1 and tn represent the start and end points of the integration interval.

S2.4 Electronic structure analysis of TCE

Supplementary quantum-chemical analysis of the TCE molecule was performed to provide molecular-level support for its interaction tendency at the BC/Fe interface. As shown in Figure 9, the ESP distribution, frontier orbitals, Hirshfeld charges, and Fukui indices together indicate that TCE possesses spatially heterogeneous electron-density features and chemically active sites. These characteristics are consistent with the interfacial configuration shown in Figure 8(c), in which TCE preferentially approaches the Fe-O coordinated region and induces local charge redistribution. Therefore, the electronic structure analysis of TCE provides supplementary molecular-level evidence for its interaction tendency with the internal active interface of BFMS.

Table S2 Specific surface area data for different m(BC):m(KOH) pore-forming ratios.

Samples	Surface area [$m^2 \cdot g^{-1}$]	Pore volume [$cc \cdot g^{-1}$]
BC	2.2572	0.030971
$BK_{0.4}$-800	602.8941	0.481932
$BK_{0.8}$-800	970.4061	0.46908
$BK_{1.2}$-800	1669.2769	0.789165
$BK_{1.6}$-800	1373.2245	0.633533
$BK_{2.0}$-800	1483.7062	0.701179
$BK_{2.4}$-800	1379.8168	0.560192

Table S3 Specific surface area data at different pore-forming temperatures.

Samples	Surface area [$m^2 \cdot g^{-1}$]	Pore volume [$cc \cdot g^{-1}$]
BC	2.2572	0.030971
$BK_{1.2}$-600	583.2169	0.289356
$BK_{1.2}$-650	646.6071	0.36263
$BK_{1.2}$-700	943.5853	0.448962
$BK_{1.2}$-750	1580.1796	0.87864
$BK_{1.2}$-800	1483.7062	0.701179
$BK_{1.2}$-850	1919.2277	1.428173
$BK_{1.2}$-900	1790.6122	1.26207

Table S4 Quantification of residual ratios and exposure loads of Cu(II) and TCE in different interactive systems

System Interaction	Type	R_{7h}	AUC	AUC_{rel}
MS-inhibitors	Cu(II)	0.868	28.535	5.349
BF-inhibitors		0.538	19.585	3.976
BFMS-inhibitors		0.454	17.424	3.455
MS-AnAOB-inhibitors		0.909	30.962	5.813
BF-AnAOB-inhibitors		0.543	20.134	3.988
BFMS-AnAOB-inhibitors		0.677	22.263	4.313
MS-inhibitors	TCE	0.871	7.062	5.482
BF-inhibitors		0.724	6.332	5.117
BFMS-inhibitors		0.884	7.467	5.449
MS-AnAOB-inhibitors		0.762	6.913	5.412
BF-AnAOB-inhibitors		0.985	8.134	5.935
BFMS-AnAOB-inhibitors		0.981	7.543	6.096

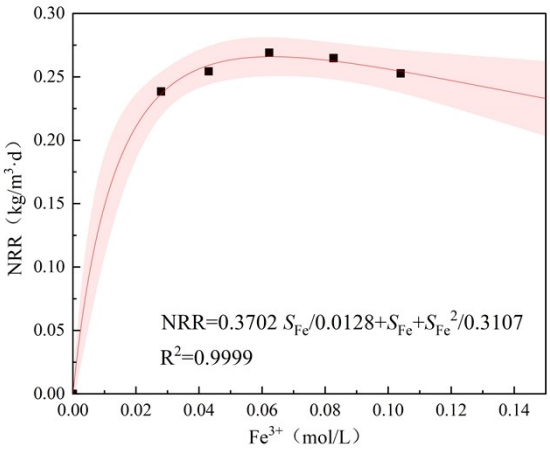

Figure S2. Kinetic curves of inhibition of nitrogen removal efficacy of Anammox at different solid-liquid ratios and Fe(III) concentrations. (The red line represents the fitted curve, and the shaded region indicates the 95% confidence interval)

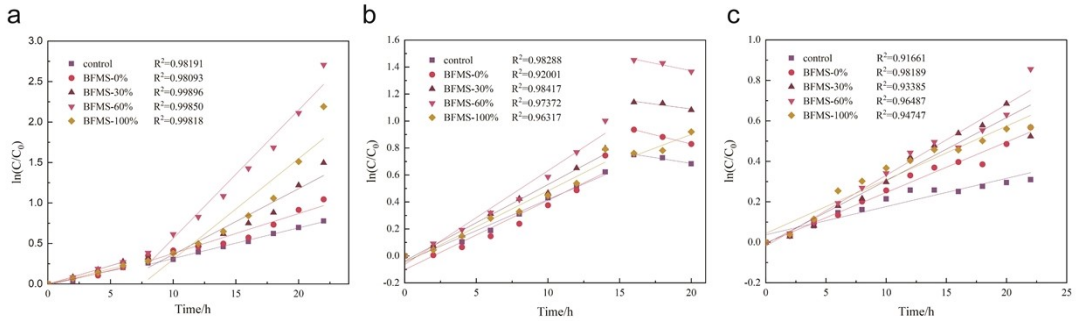

Figure S3. Kinetic fitting of Anammox systems with BFMS-*x* (*x* = 0%, 30%, 60%, 100%): (a) Enrichment, (b) Cu (II), (c) TCE.

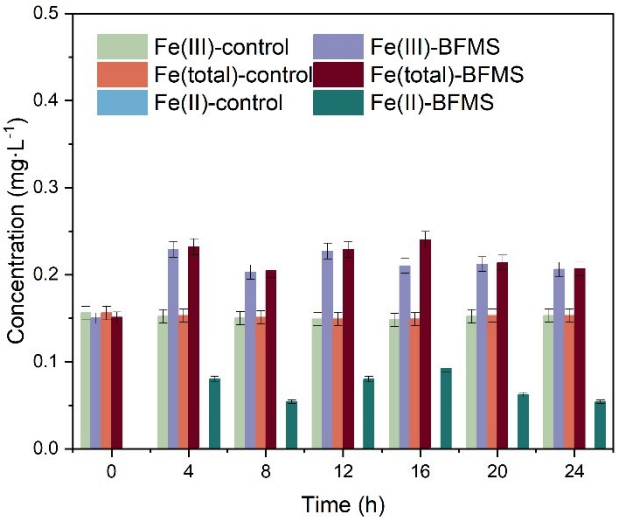

Figure S4. Concentrations of soluble Fe leached from BFMS over the 24 h reaction period.

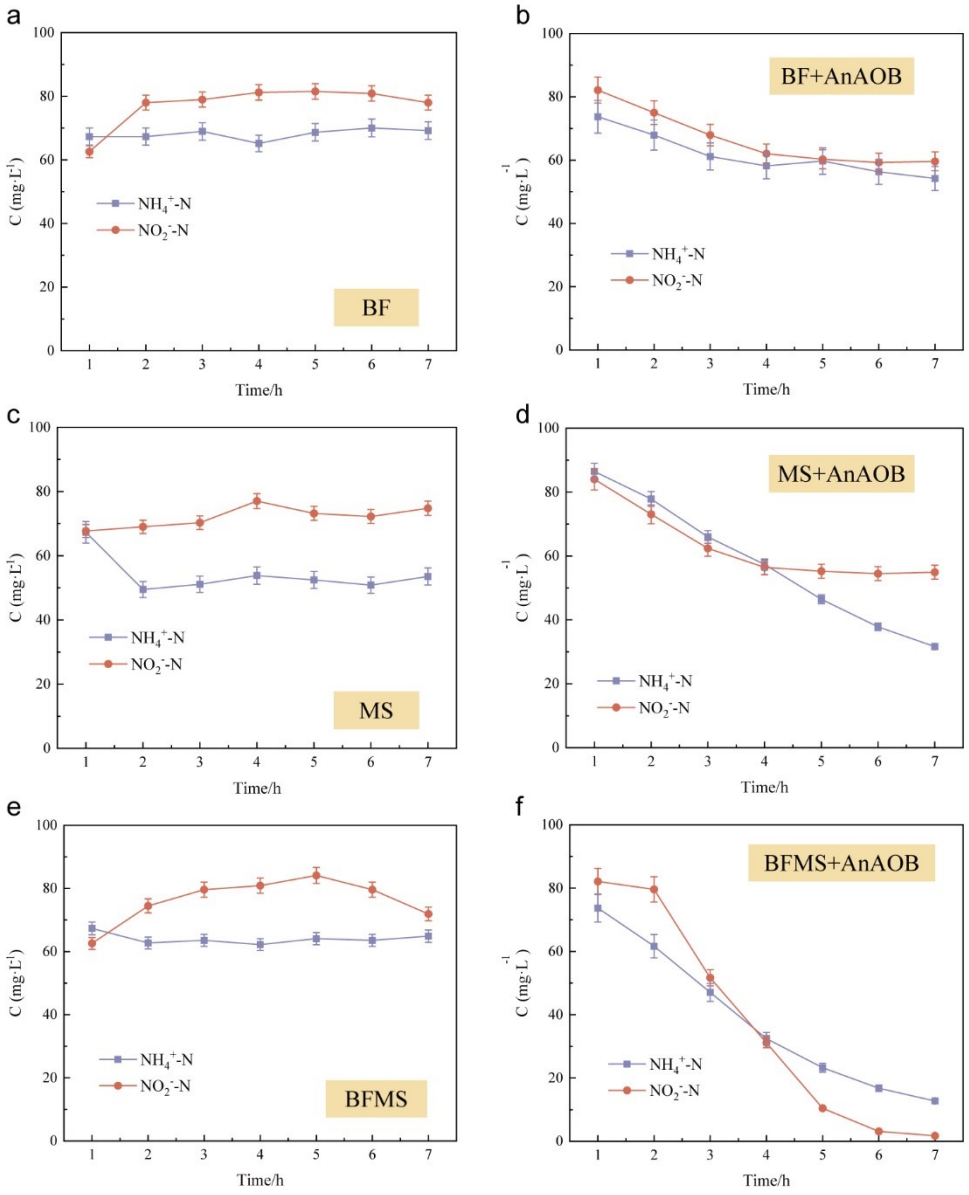

Figure S5. Substrate concentrations in different interacting systems under Cu(II)-TCE combined stress: (a) BF; (b) BF+AnAOB; (c) MS; (d) MS+AnAOB; (e) BFMS; (f) BFMS+AnAOB.

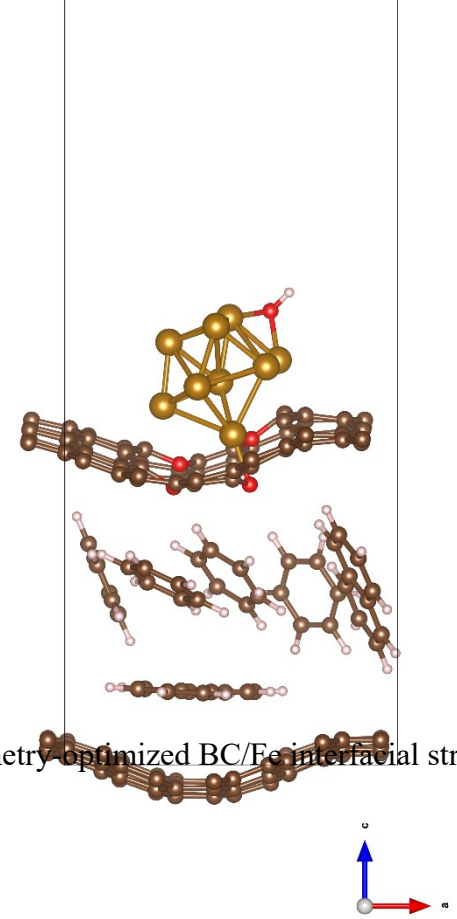

Figure S6. Geometry-optimized BC/Fe interfacial structure in BFMS.

References

［1］ APHA. Standard methods for the examination of water and wastewater, 21st ed [S]. 2005.

[2] Zielińska M, Cydzik-Kwiatkowska A, Kulikowska D, et al. Iron-containing carriers stimulate nitrogen conversions in one-stage reactors treating N-rich digester supernatant[J]. Journal of Environmental Chemical Engineering, 2023, 11(1): 109115.

[3] Test methods of wooden activated carbon-Determination of iron content GB/T-12496.19-2015 [S]. State General Administration of the People"s Republic of China for Quality Supervision and Inspection and Quarantine, Standardization Administration of the People’s Republic of China, 2015.

[4] Ni B-J, Chen Y-P, Liu S-Y, et al. Modeling a granule-based anaerobic ammonium oxidizing (ANAMMOX) process[J]. Biotechnology and Bioengineering, 2009, 103(3): 490-499.

[5] He C-K, Hung M-C, Hxu C-H, et al. Pitfalls in measuring solution toxicity using the level of bioluminescence inhibition in Aliivibrio fischeri[J]. Comparative Biochemistry and Physiology Part C: Toxicology & Pharmacology, 2025, 287: 110067.